Biomass Conversion and Biorefinery
https://doi.org/10.1007/s13399-022-03304-4

ORIGINAL ARTICLE

Dye removal using novel adsorbents synthesized from plastic waste and eggshell: mechanism, isotherms, kinetics, thermodynamics, regeneration, and water matrices

Kenneth Mensah[1] · Hatem Mahmoud[1,2] · Manabu Fujii[3] · Mahmoud Samy[4] · Hassan Shokry[1,5]

Received: 21 June 2022 / Revised: 2 September 2022 / Accepted: 13 September 2022

Abstract

High-density polyethylene (HDPE) waste and chicken eggshell were used to synthesize three novel adsorbents, namely mesoporous graphene (MG), nano-eggshell modified graphene (nEMG), and nano-magnetic eggshell modified graphene (nM-EMG) for methyl red (MR) adsorption from simulated wastewater. The effects of adsorption conditions (pH, contact time, initial dye concentration, adsorbent dose, and temperature) were investigated. MG, nEMG, and nM-EMG were characterized using SEM, TEM, BET, EDX, XRD, and FTIR analyses. MG, nEMG, and nM-EMG had specific surface areas of 15, 31, and 179 m^2/g and mean pore diameters of 27, 29, and 5 nm respectively. The equilibrium adsorption capacities of MG, nEMG, and nM-EMG were 5.6, 8.1, and 6.5 mg/g respectively at MR concentration of 100 mg/L, pH 4, adsorbent dose of 1.0 g/100 mL, and temperature of 25 °C. All MR sorption processes followed the pseudo-second-order and Langmuir–Freundlich model. The adsorption rates were controlled by intra-particle and film diffusion. MR uptake on the synthesized adsorbents was spontaneous, endothermic, and chemisorption. The adsorption occurred via electrostatic interactions, π electron interactions, and hydrogen bonding. The performance of the prepared adsorbents was examined in different water matrices and compared with other MR adsorbents. After five regeneration cycles, the adsorbent reusability study showed that nM-EMG is the most stable and reusable adsorbent.

Keywords Dye adsorption · Eggshell · Graphene · Magnetic adsorbent · Plastic waste · Wastewater treatment

1 Introduction

Azo dyes, characterized by one or more azo (–N = N–) groups in their structure, are the most widely used synthetic dyestuffs [1]. These synthetic dyes are used in the textile, paper, leather, plastic, and cosmetic industries [2]. The extensive utilization of azo dyes implies the generation of large quantities of dye-containing wastewaters which can adversely impact the environment [1]. Aromatic azo dyes like methyl red (MR) are bio-recalcitrant pollutants that cannot be easily degraded and remain in the environment for long periods [1]. MR is also mutagenic, eye, skin, and digestive tract irritant and poses a severe threat to life [3].

Wastewater treatment processes must involve highly efficient and cost-effective methods [3]. Biological treatment, photocatalysis, reverse osmosis, precipitation, electrocoagulation, and ion exchange are conventional wastewater treatment methods [4]. However, these methods have some major disadvantages such as the production of toxic by-products, as well as the complexity and high cost [5]. On the other

✉ Kenneth Mensah
kenneth.mensah@ejust.edu.eg

1 Environmental Engineering Department, Egypt-Japan University of Science and Technology, New Borg El-Arab City, Alexandria, Egypt

2 Department of Architecture Engineering, Faculty of Engineering, Aswan University, Aswan 81542, Egypt

3 Department of Civil and Environmental Engineering, Tokyo Institute of Technology, Meguro-ku, Tokyo 152-8552, Japan

4 Department of Public Works Engineering, Faculty of Engineering, Mansoura University, Mansoura 35516, Egypt

5 Electronic Materials Research Department, Advanced Technology and New Materials Research Institute, City of Scientific Research and Technological Applications (SRTA-City), Alexandria, Egypt

Published online: 24 September 2022

hand, adsorption, another conventional wastewater treatment method, presents an eco-friendly process of wastewater decontamination without generating any toxic by-products [6]. Moreover, the adsorption method is easy to operate and requires low capital and operational cost. However, adsorption technology has drawbacks including the high cost of adsorbents and the time-consuming regeneration procedure [7].

Recent studies have focused on the feasibility of using low-cost precursors such as agro-waste due to the cost of disposing spent adsorbents [8–11]. Such precursors must have high purity, rich in carbon and volatiles, and be widely available [12]. Meanwhile, plastics like high-density polyethylene (HDPE) are made from fossil sources [13]. HDPE contains a high amount of carbon (85%) and volatile matter (99%), making them an excellent precursor for producing carbon adsorbents [14]. Moreover, plastics like HDPE are widely available as cosmetic containers and drinking bottles with short one-time usage, thus forming a major constituent of municipal and domestic solid waste and currently are a severe environmental menace due to their resistance to natural degradation [15].

Global egg production is estimated to be approximately 77 million tons per year, resulting in over a million tons of eggshell biomass generated as waste [16]. Eggshell contains a high biomineral content (94% calcium carbonate), 4% organic substances, 1% calcium phosphate, and 1% magnesium carbonate [17, 18]. Biomaterials like eggshells are highly porous with high surface area and surface functional groups [17, 19]. Studies have shown that eggshells can remove heavy metals and organic pollutants from aqueous solutions [20–23]. However, the reusability of eggshells can be enhanced by compositing them with other materials [24, 25]. Furthermore, converting eggshells into nanoparticles and modifying adsorbents with eggshell nanoparticles can also enhance the surface area, porosity, and functional groups of absorbents [17, 26]. Hence, modifying adsorbents with eggshells can improve the adsorbents' capacity and affinity for adsorbates. Moreover, it can offer a low-cost and green technique for enhancing adsorbents' properties.

Meanwhile, the ability and ease of reusing adsorbents are vital to the economics of their application [27]. Magnetization of adsorbents offers a simple method for recovering spent adsorbents from solutions using an external magnet [7]. Magnetization reduces the time and energy required to recover adsorbents through filtration and centrifugation [28]. Moreover, the magnetization of adsorbents with nano-magnetic metal oxide compounds like magnetite nanoparticles (nano-Fe_3O_4) can enhance the diffusion of organic pollutants towards the adsorbent surface [7, 29].

This work presents the conversion of plastic waste (HDPE) and chicken eggshell to a novel, low-cost carbon nano-eggshell-based adsorbent for MR removal from simulated wastewater. Additionally, the nano-eggshell graphene composite was functionalized with magnetite nanoparticles and an in-depth study was performed to ascertain the adsorption behaviors and adsorbents' reusability. A detailed analysis of the adsorption conditions, mechanism, kinetics, isotherms, thermodynamics, and reusability was conducted. An assessment of the quality of the prepared adsorbents compared with other adsorbents produced for MR adsorption was evaluated. Finally, the performance of the prepared adsorbents in different water matrices was assessed.

2 Materials and experimental methods

2.1 Materials and reagents

HDPE waste from cosmetic products and drinking bottles were gathered from domestic and municipal solid waste. Chicken eggshells were collected from a local restaurant. Pure grade MR (Fig. S1) and ferrous chloride tetrahydrate (reagent salts 99%, $FeCl_2.4H_2O$) were procured from Agros Organics in Belgium. Ferric chloride hexahydrate (extra pure 97%, $FeCl_3.6H_2O$) was purchased from LOBA Chemie in India. N,N-Dimethylformamide (DMF) (ACS reagent 99.8%, C_3H_7NO) and hydrochloric acid (ACS reagent 37%, HCl) were purchased from Merck KGaA in Germany. Ethanol (70%, C_2H_5OH) was obtained from Brand Chemicals in Egypt. Sodium chloride (85% NaCl) was procured from Alpha Chemika in India. Sodium hydroxide pellet (98%, NaOH) was purchased from Piochem in Egypt. Demineralized water was purchased from Hach in the USA.

2.2 Preparation of adsorbents

Waste HDPE plastics were shredded, washed with distilled water, and dried. A 420-mL stainless steel autoclave was loaded with the dried plastics, firmly sealed, and subsequently the autoclave was transferred to a muffle furnace (ASH AMF 25 N, Japan). The furnace temperature was adjusted to 600 °C at 27 °C/min heating rate. The temperature was maintained for 2 h and left to cool overnight. The char product (MG) was weighed to calculate the product yield using Eq. 1.

$$\text{Yield} = \frac{\text{weight of MG}}{\text{Dry weight of HDPE precursor}} \times 100\% \quad (1)$$

The eggshell nanoparticles were prepared at 1 g eggshell/100 mL DMF via a mechanical-sonochemical method described in our previous study [26]. The nano-eggshell impregnated MG composite (nEMG) was prepared using the high-temperature impregnation method [30]. One gram

of MG was added to the nano-eggshell suspension and the mixture was stirred at 70 °C for 2 h. Both the white color of eggshell nanoparticles and the black color of carbon were seen at the start of stirring. The black and white colors vanished during the mixing process, leaving only one gray color. This was seen as evidence of interaction between the MG and eggshell nanoparticles. The final mixture was filtered, and the residue was oven-dried at 110 °C overnight to produce nEMG.

1.4 g $FeCl_3.6H_2O$ and 0.5 g $FeCl_2.4H_2O$ were dissolved in 100 mL of demineralized water under stirring to produce at a solution of 50 mM $FeCl_3.6H_2O$ and 25 mM $FeCl_2.4H_2O$. One gram of nEMG was added to the resultant solution. Drops of 1 M NaOH were added to the mixture until the formation of a black precipitate in a co-precipitation process as illustrated in Eq. 2 [31]. The resultant precipitate was vacuum filtered and thoroughly washed with demineralized water and ethanol. The prepared cake was dried at 110 °C for 2 h and the dried cake (nM-EMG) was crushed. All prepared adsorbents were kept in a Pyrex desiccator immediately after preparation.

$$Fe^{2+} + 2Fe^{3+} + 8OH^- = Fe_3O_4 + 4H_2O \quad (2)$$

2.3 Characterization of prepared adsorbents

Surface morphological studies of the prepared adsorbents were performed using a scanning electron microscope (SEM) (JEOL, JSM-6010LV, Japan). High-resolution micrographs of the morphology and elemental content of the produced adsorbents were obtained using a transmission electron microscope (TEM) equipped with energy dispersion X-ray spectroscopy (EDX) (JEOL, JEM-2100F, Japan). Bruker D2 Phaser was used to generate X-ray diffraction (XRD) crystallographic information of the prepared adsorbents. The surface functional groups of the adsorbents were determined by Fourier transform infrared spectroscopy (FTIR) (Shimadzu FTIR-8400S Spectrometer, Japan). The N_2 adsorption–desorption isotherm, BET surface area, and pore distribution of the prepared adsorbents were investigated with Microtrac MRB Belsorp Mini X, Japan.

2.4 Point of zero charge

Fifty milliliters of mixtures containing 0.1 M NaCl and 0.2 g of MG, nEMG, and nM-EMG was prepared for point of zero charge (pH_{pzc}) determination using the pH drift method. 0.1 M NaOH and 0.1 M HCl were used to adjust the pH of the mixtures to the values of 2, 4, 6, 8, and 10. The mixtures were stirred at room temperature for 24 h to achieve equilibration. The final pH was measured and plotted against the initial pH to estimate the pH_{pzc}. All pH measurements were done with Adwa AD8000 bench meter.

2.5 Adsorption experiments

Stock solutions of 500 mg/L MR dye were prepared by dissolving 0.5 g of solid MR dye in 100 mL of ethanol and then topped up with 900 mL of distilled water. Desired concentrations of 100 mL MR solution were prepared by diluting the MR stock solution with an appropriate volume of deionized water. MR adsorption parameters such as pH (2–10), contact time (0–120 min), initial dye concentration (10–200 mg/L), adsorbent dose (1–20 mg/mL), and temperature (25–60 °C) were examined at an agitation speed of 500 rpm. The pH of the MR solution was adjusted with 0.1 M HCl and 0.1 M NaOH solutions. The temperature of the MR solution was adjusted using a magnetic stirrer/hot plate (WiseStir digital hotplate stirrer). After adsorption, the supernatant was centrifuged at 6000 rpm for 10 min and the concentration of MR was evaluated using UV–vis spectrophotometer (Jasco V-630 spectrophotometer, Japan) at 497 nm [32]. All experiments were conducted in triplicate and the average values with their corresponding standard deviations were plotted. The formulas for the amount and percentage of MR adsorbed onto the prepared adsorbents and the details of the adsorption isotherms, kinetics, and thermodynamics models are explained in Text S1.

2.6 Regeneration of spent SG, AG, and NFMAG

After each successive MR adsorption cycle, the adsorbents were separated from the solution and rinsed with demineralized water. MG and nEMG were recovered from solution by filtration and centrifugation at 6000 rpm for 10 min, while nM-EMG was recovered using an external magnet. The loaded adsorbents were eluted with 60 mL of ethanol at 30 °C. The dispersions were stirred at 500 rpm for 2 h for MR desorption. Finally, the adsorbents were separated, washed with demineralized water, and dried at 110 °C for 1 h for reuse.

3 Results and discussion

3.1 Characteristics of prepared adsorbents

3.1.1 Morphological structure of prepared adsorbents

SEM micrograph of MG shows amorphous structures with irregular shapes and sizes (Fig. 1a). The large void in MG depicts a highly porous carbon material. The different sized morphologies of MG suggest a gradual depletion of material, most likely due to activation affecting both

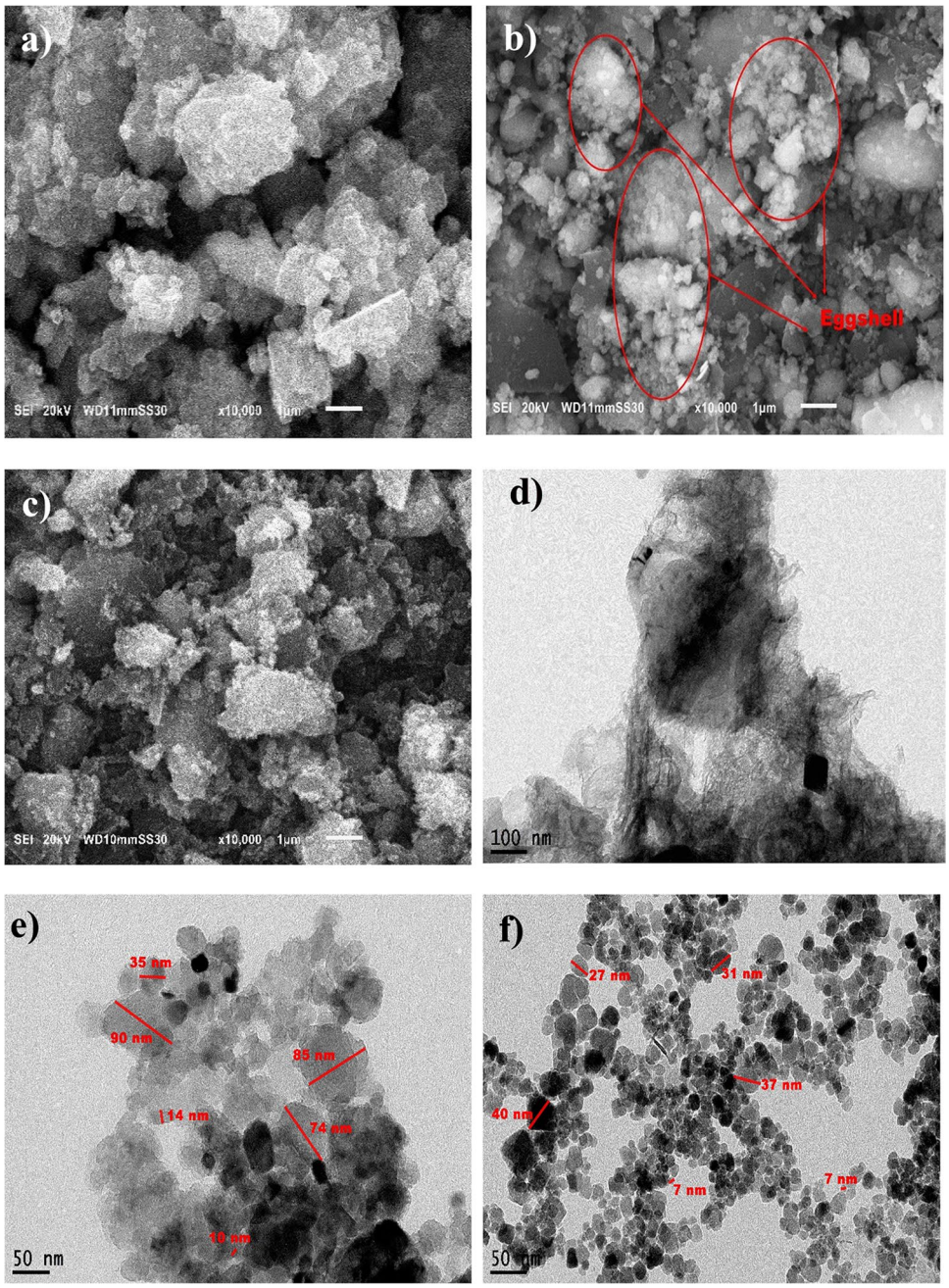

Fig. 1 SEM micrographs of **a** MG, **b** nEMG, and **c** nM-EMG and TEM micrographs of **d** MG, **e** nEMG, and **f** nM-EMG

the surface and the inside of the material [33]. Meanwhile, the SEM image of nEMG shows a rugged surface due to the uniform interaction between the eggshell nanoparticles and MG (Fig. 1b). nM-EMG exhibits a rougher surface due to the coating of iron oxides on the precursor nEMG matrix (Fig. 1c). TEM micrograph of MG reveals shadows of agglomerated rippled graphene sheets entangled with each other (Fig. 1d). Dark portions suggest graphite deposits (Fig. 1d). TEM micrograph of nEMG shows eggshell nanoplatelets with sizes between 10 and 90 nm uniformly dispersed on the graphene matrix (Fig. 1e), confirming the successful preparation of nEMG. TEM image of nM-EMG reveals sphere-like iron oxide nanoparticles with diameters ranging from 7 to 40 nm (Fig. 1f). Hence, nEMG was an excellent support material for magnetization since the iron oxides retained the nanometric sizes [34]. Uniformly dispersed dark portions in Fig. 1f are graphene and eggshell deposits from the precursor nEMG.

3.1.2 Texture of prepared adsorbents

The N_2 adsorption and desorption isotherm curves of MG and nEMG (Fig. 2a) show increasing N_2 sorption at high relative pressures, typical of type-III isotherm according to

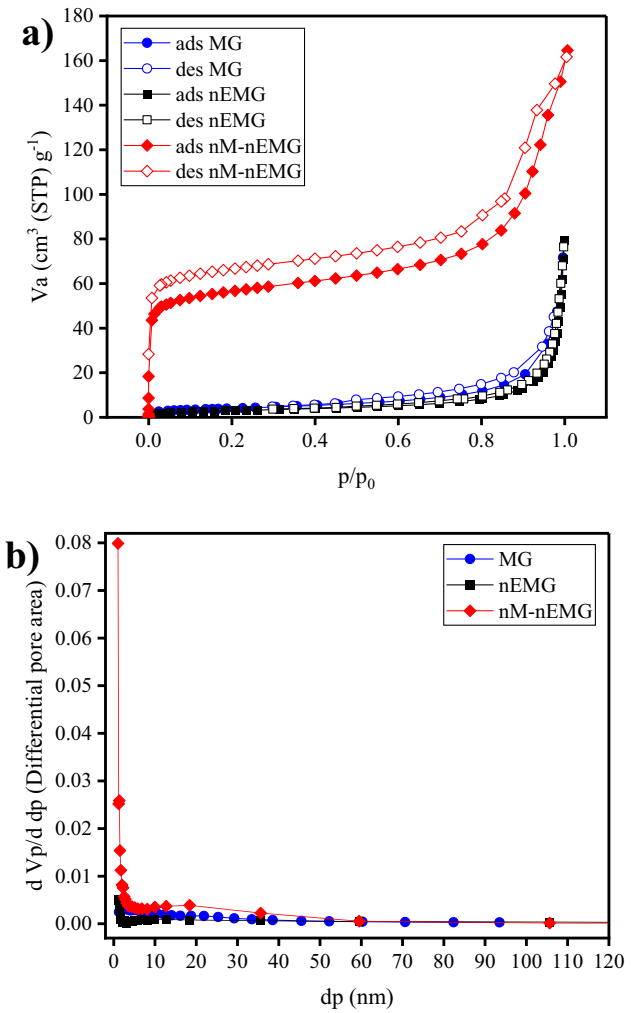

Fig. 2 **a** N2 adsorption–desorption isotherms and **b** pore volume distribution of prepared adsorbents

Table 1 Textural analysis of prepared adsorbents

Adsorbent	BET surface area (m^2/g)	Mean pore diameter (nm)	Total pore volume (cm^3/g)
MG	15	27	0.098
nEMG	31	29	0.099
nM-EMG	179	5	0.233

IUPAC classification [35]. The type-III isotherm depicts a mesoporous texture of MG and nEMG [35, 36]. Regarding nM-EMG, the N_2 sorption isotherm represents a type-II isotherm (Fig. 2a) which typically has unrestricted monolayer-multilayer adsorption up to high relative pressure (p/p_0) and a mesoporous structure [35, 36]. The BET surface area of MG (15 m^2/g) increased after modification with nano-eggshell to form nEMG (31 m^2/g) (Table 1). Nanometric eggshell platelets are highly porous materials with relatively high specific surface area than micro-sized eggshell powder; hence, the eggshell nanoparticles enhanced the total surface area of nEMG [17, 26]. As presented in Table 1, the specific surface area (179 m^2/g) and pore volume of nM-EMG increased due to magnetite nanoparticles' relatively high inherent surface area [37]. The pore distributions of MG and nEMG show broadly distributed pores between 2 to 60 nm and 2 to 100 nm respectively (Fig. 2b). Meanwhile, the pore diameter of nM-EMG is distributed below 20 nm due to the nano-Fe_3O_4 coating (Fig. 2b). The mean pore diameters of MG, nEMG, and nM-EMG are 27, 29, and 5 nm respectively.

3.1.3 Elemental analysis of MG, nEMG, and nM-EMG

EDX spectroscopy was used to explain the various modifications in the prepared adsorbents by determining the differences in their elemental compositions. MG is a high purity carbon material with strong peaks of carbon and oxygen (Fig. 3a). After modification of MG with nano-eggshell, calcium peaks appeared with carbon and oxygen in nEMG spectra (Fig. 3b). This indicates that the eggshell bio-$CaCO_3$ nanoplatelets were successfully loaded on the matrix of MG to form nEMG. Meanwhile, EDX spectra of nM-EMG show iron peaks with a relatively high amount of oxygen (Fig. 3c) due to iron oxide coating.

3.1.4 Crystallographic analysis of MG, nEMG, and nM-EMG

The XRD spectra of all prepared adsorbents are shown in Fig. 4. The graphitization of MG is observed by the peaks at $2\theta°$ of 24.25° and 43.77° corresponding to the (002) and (101) planes of graphene respectively (JCPDS card no. 87–1526). The (101) graphitic plane depicts a stacking order of graphene sheets [33]. The graphene peaks of MG are broad with an interlinear spacing of 3.67 Å (higher than the 3.44–3.55 Å of regular crystalline graphene) indicating an amorphous graphitic structure [38]. Such amorphous graphene formation is ascribed to the termination of sp2 bonds of carbon atoms or intercalation of the hexagonal planar units by oxygen which disrupts any order in the graphitic plane [38]. In nEMG, the peaks at $2\theta°$ of 23.2°, 29.16°, 36°, 39.6°, 43°, 47.5°, 48.51°, 57.4°, 60.77°, and 64.93° correspond to the (012), (104), (110), (113), (202), (016), (018), (122), (224), and (036) diffraction planes of calcite (JCPDS card no. 47–1743) [17, 25]. Calcite is the most stable polymorph of $CaCO_3$ and the presence of strong peaks of calcite in nEMG also confirms the successful loading of eggshell nanoplatelets onto MG [25, 39]. These strong peaks also reveal that no structural changes in the eggshell $CaCO_3$ occurred during the nano-eggshell preparation [17]. The peak at 26.55° $2\theta°$ is attributed to precursor MG's (002)

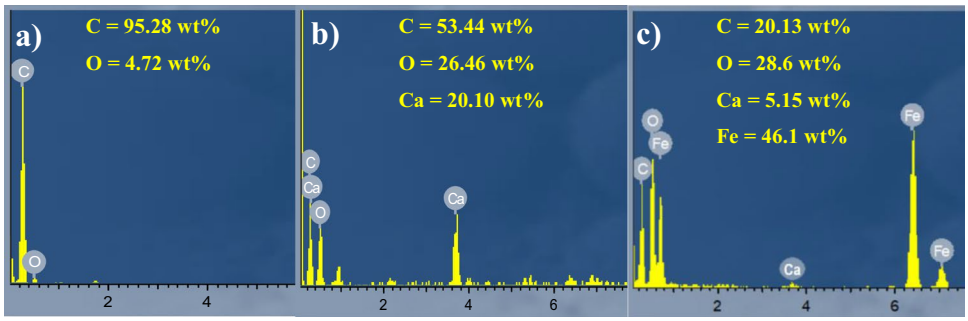

Fig. 3 EDX spectra of **a** MG, **b** nEMG, and **c** nM-EMG

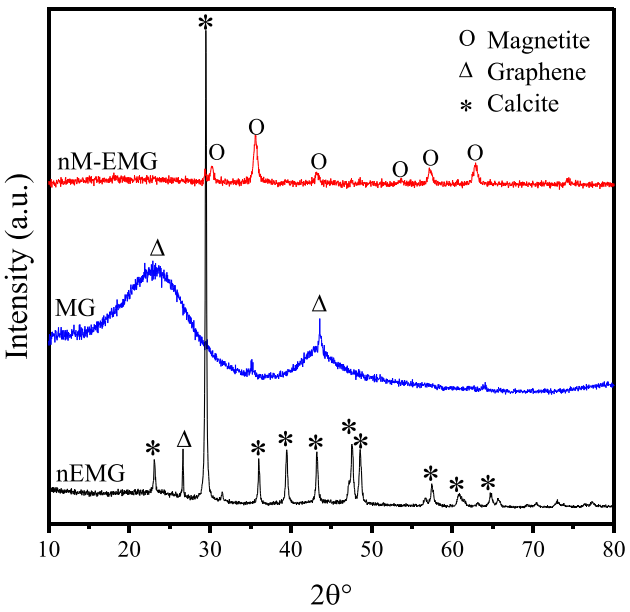

Fig. 4 XRD spectra of prepared adsorbents

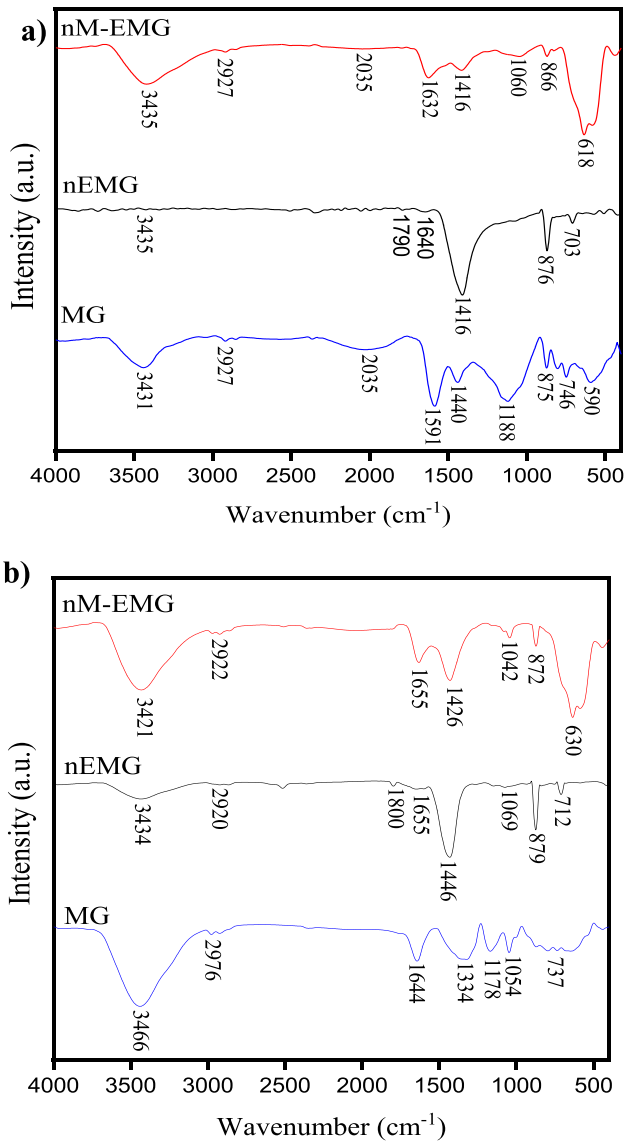

Fig. 5 FTIR of prepared adsorbents **a** before and **b** after MR adsorption

graphitic plane [7]. For nM-EMG, the peaks at 30.27°, 35.56°, 43.29°, 53.72°, 57.27°, and 63.84° correspond to the (202), (311), (400), (422), (511), and (440) reflection planes of magnetite (Fe_3O_4) respectively (JCPDS card no. 19–0629) [29, 37]. The existence of magnetite peaks further confirms the successful ferro-magnetization of nM-EMG.

3.1.5 FTIR spectra before and after adsorption

The FTIR spectra of the prepared adsorbents before MR adsorption, as presented in Fig. 5a, affirmed the successful adsorbent preparations. The peaks at 1591, 1632, and 1640 cm^{-1} are attributed to the vibrations of C = C stretching of aromatic rings of sp2 graphite in all prepared adsorbents [7]. The intensity of the C = C peak was reduced in nEMG and nM-EMG due to surface coating by eggshell and magnetite nanoparticles respectively. The peaks at 3431 and 3435 cm^{-1} in MG, nEMG, and nM-EMG are characteristic of O–H stretching vibration of polymeric compounds such as alcohols, carboxylic acids, and phenols, indicating the existence of free hydroxyl groups. The peaks at 2927, (2035, 1416, and 1440), and (1060 and 1188) cm^{-1} in MG and nM-EMG correspond to C–H, C = O, and C–O vibrations

of methyl, carboxyl, and alkoxyl groups respectively. The peaks at 866, 875, 746, and 590 cm^{-1} are due to out-of-plane angular deformation of aromatic rings in MG and nM-EMG. However, the strong peak at 618 cm^{-1} in nM-EMG is attributed to Fe–O bond stretching vibrations of magnetite (Fe_3O_4) [34]. Regarding nEMG, the weak peak at 1790 cm^{-1} corresponds to the C = O bonds of carbonates (bio-$CaCO_3$ in eggshell). The peak at 703 cm^{-1} is ascribed to Ca–O bond [20]. Meanwhile, the peaks at 1416 cm^{-1} and 876 cm^{-1} correspond to the C–O stretching and bending modes of $CaCO_3$ respectively [22, 40, 41]. Hydrophilic compounds such as O–H and Fe–O promote efficient adsorbent dispersion in water, while hydrophobic groups such as C = C increase contaminant binding affinity [34].

Changes in FTIR spectra of the adsorbents after MR adsorption (Fig. 5b) were used to explain the MR sorption behavior and the role of adsorbents' surface functional groups. Distinct changes in the wavenumber and intensity of the initial O–H, C = O, and C–O peaks show the involvement of the oxygen functional groups of the prepared adsorbents in MR adsorption. The peaks at 3421, 3434, and 3466 cm^{-1} in all the adsorbents can be attributed to the stretching vibrations of O–H groups of MR or lattice water. The C = C bond peaks in all the prepared adsorbents shifted to a higher wavenumber of 1644 and 1655 cm^{-1} due to π–π electron stacking of the C = C bonds of the MR dye's benzene rings and the delocalized electron in the prepared graphene-based adsorbents [29, 42, 43]. The peaks at 2922, 2920, and 2976 cm^{-1} are due to the stretching vibration of the C–H groups of MR. The peaks at around 1426 and 1334 cm^{-1} can be ascribed to the bending vibration of C = O (carbonyl group) of MR, whereas the peaks at 1178, 1054, 1069, and 1042 cm^{-1} are attributed to the stretching vibration of C–O bonds of anionic MR [7, 43]. The presence of 1800, 1446, 879, and 712 cm^{-1} peaks of $CaCO_3$ in nEMG indicates the stability of the calcite in the MR solution. The Fe–O peak of nM-EMG shifted to a higher wavenumber of 630 cm^{-1}, suggesting a possible role in assisting organic molecules' diffusion to the active sites [29]. Based on the FTIR findings, we proposed that the interaction between MR molecules and the prepared adsorbents were (i) π-π electron interactions between the aromatic groups of MR and graphene, (ii) electrostatic interactions between COO^- group of MR and the oxygen functional groups of the adsorbents, and (iii) hydrogen bonding with COOH group of MR as illustrated in Fig. 6.

3.1.6 pH_{pzc} of prepared adsorbents

The pH of the adsorbate solution can alter the surface charge of adsorbents through protonation and deprotonation interactions with H_3O^+ and OH^- ions [27, 44]. pH_{pzc} is the pH at which the adsorbent's surface is electrically neutral [44]. The pH_{pzc} of MG, nEMG, and nM-EMG are 7.2, 8.5, and 6.8 respectively (Fig. S2). Since MG has a pH_{pzc} of 7.2 and nEMG is a composite of MG and nano-eggshell, the increase in the pH_{pzc} value of nEMG to 8.5 was due to the inclusion of eggshell. Annane et al. [20] reported that eggshell has a pH_{pzc} of 9.27. Kumi also reported an increase in pH_{pzc} to 8.2 after modifying sludge-derived biochar with eggshell [45]. The reduction in the pH_{pzc} value of nM-EMG is due to the additional surface oxygen content from the iron oxide nanoparticles.

3.2 Adsorption studies

3.2.1 Effect of initial MR solution pH

MR is an azo dye (2-(N,N-dimethyl-4-aminophenyl) azobenzenecarboxylic acid) soluble in water with a pK_a of 5.1 and can exhibit hydrophobic interactions due to its $–N(CH_3)_2$ sites [43, 46]. MR has complex acid–base equilibria with four different forms depending on solution pH. These forms include neutral (MR^0), zwitterionic ($MR^{\pm}$), protonated/cationic (MRH^+), and deprotonated/anionic (MR^-) [47]. Therefore, we first investigated the effect of pH to ascertain the optimum adsorption pH as depicted in Fig. 7.

At the pristine pH of MR solution (6.1), which is above the MR pK_a and MR exists as MR^- because of the deprotonation of its carboxylic (–COOH) group to COO^-, MG exhibited a relatively high MR adsorption capacity (4.39 mg/g) than nEMG (2.97 mg/g) and nM-EMG (2.27 mg/g). Higher MR adsorption occurred between protonated MG and

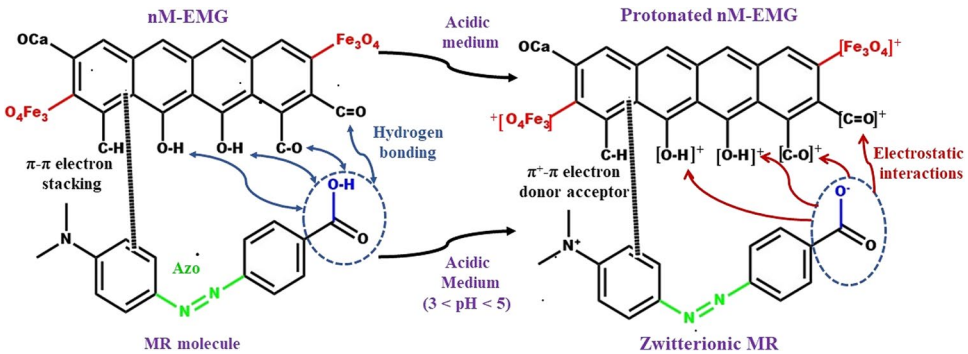

Fig. 6 Plausible MR adsorption mechanism showing interactions between functional groups of nM-EMG and MR

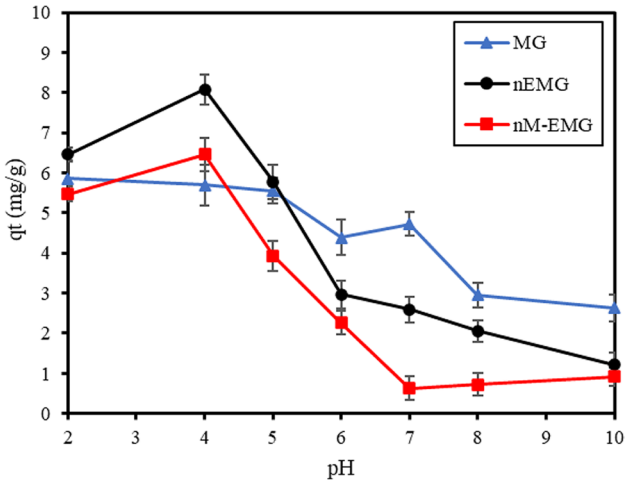

Fig. 7 Effect of pH on MR decolorization [conditions: $C_0 = 100$ mg/L; adsorbent dose = 1 g/100 mL; solution temperature = 25 °C, contact time = 60 min]

deprotonated or anionic MR at pH 6.1. Moreover, MG can interact with MR over a wide pH range via π-π electron interactions. nEMG has a pH_{pzc} of 8.5, which implies that its net surface charge becomes positive below 8.5 and negative beyond that value. However, the lower adsorption in nEMG may be due to the basic carbonate species from calcite which created a basic environment causing the final pH to rise to 7.8 and a repulsion between MR^- and nEMG [48]. Meanwhile, nEMG contains 50% graphene (1:1 carbon:eggshell nanoparticles), which could also adsorb MR over a wide pH range via π-π electron interactions. Regarding nM-EMG, it is suggested that the MR had a weak electrostatic interaction with the Fe_3O_4 sites in the adsorbent at pH 6.1 due to resonance leading to low adsorption capacity [46]. MR adsorption capacities declined significantly with increasing solution pH > 7 due to deprotonation of adsorbent surfaces by hydroxyl ions $[OH]^-$ resulting in repulsive forces between the COO^- group of MR^- and negatively charged adsorbents. In mildly acidic conditions (3 < pH < 6) which is below the pK_a of MR, the $-N(CH_3)_2$ group of MR becomes protonated [47]. Thus, MR usually exists as zwitterionic $MR^{\pm}$ with $-[N(CH_3)_2]^+$ and COO^- groups in mildly acidic conditions while adsorbents' surface is more protonated based on their pH_{pzc} [47]. Consequently, the MR adsorption was favored at these low pH ranges, where strong electrostatic interactions occurred between the COO^- group of $MR^{\pm}$ and the positively charged adsorbents' surface. nEMG had the highest MR removal at pH 4. The activated (protonated) O–H, C = O, and C–O functional groups of the high surface area nEMG supplemented its graphene component and enhanced nEMG adsorption affinity for the COO^- group of $MR^{\pm}$ [40, 41, 48]. This phenomenon explains the relatively high adsorption capacity of nEMG (8.1 mg/g) at pH 4. Moreover, the bio-$CaCO_3$ of eggshell could have also taken up MR molecules through biosorption. However, below pH 4, the adsorption capacity of nEMG declined, possibly due to the loss of adsorbent via $CaCO_3$ dissolution in the presence of excess HCl or repulsive forces between MRH^+ and positively charged nEMG surface [49]. The adsorption capacity of nM-EMG also increased significantly with decreasing pH. The highly porous nano-Fe_3O_4 in nM-EMG can also undergo protonation in acidic conditions to promote electrostatic interactions and enhance the diffusion and adsorption of MR molecules, hence its relatively high adsorption capacity (6.46 mg/g) at pH 4 compared to MG (5.6 mg/g) [7, 29, 46]. However, nano-Fe_3O_4 could gradually dissolve in strongly acidic conditions to cause adsorbent loss and thence reduce the MR adsorption efficiency at pH < 4 [28, 50, 51]. MR adsorption on MG was favored in all acidic conditions. Besides the electrostatic interactions that took place, it is possible that π^+–π electron donor–acceptor interactions between $[MG]^+$ and $MR^{\pm}/MRH^+$ also occurred even in highly acidic conditions (pH < 4). The cationic $-[N(CH_3)_2]^+$ group attached to the aromatic ring of MR may have a strong electron-withdrawing ability (highly electrophilic), causing the π electrons in the aromatic ring of $MR^{\pm}/MRH^+$ to be polarized and decreasing electron density [52]. This led to a simultaneous reduction in the electrostatic repulsion between the π electrons of MR aromatic rings and promoted the interactions between the polarized aromatic MRH^+ and the electron-rich aromatic rings of graphitic $[MG]^+$ in extremely low pH [52–54]. However, it is possible that most of the adsorptive sites of the low surface area of MG were occupied at $pH < pH_{phz}$; hence, a further decrease in pH ($pH << pH_{phz}$) did not significantly increase the adsorption capacity. It is concluded from these findings that pH 4 was the optimum pH for MR adsorption on nEMG and nM-EMG, with removal efficiencies of 71% and 64.6% respectively. Although MR adsorption on MG was favorable under all acidic conditions, pH 4 with a removal efficiency of 57% was also chosen as the optimal pH for MG since no substantial increment in MR removal efficiency was observed at pH 2 (~ 59% MR removal). The optimal pH of 4 was maintained for all subsequent experiments.

3.2.2 Effect of contact time

The MR adsorption was rapid in the first 30 min (Fig. 8). The porous texture of MG and nEMG accelerated the diffusion and adsorption of MR into these adsorbents' inner pores. After the initial 30 min, the sorption rate and intensity were reduced due to filling vacant sites. MR adsorption on MG attained equilibrium after 30 min. The nano-eggshell component of nEMG continued the MR for an extra 10 min leading to a 40-min equilibrium time for nEMG. MG is mesoporous, and MR rapidly diffuses into its inner

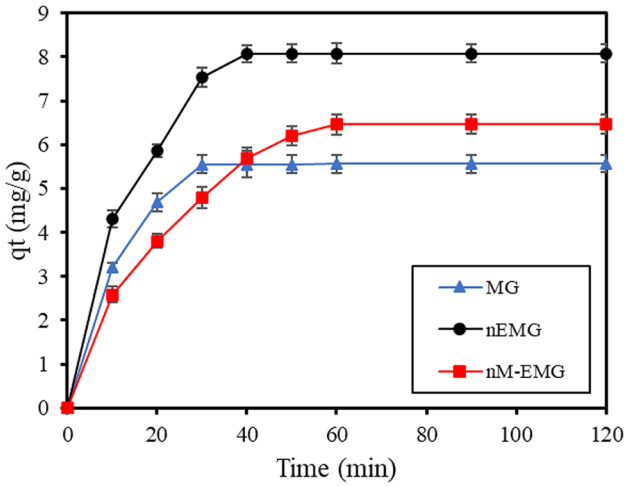

Fig. 8 Effect of contact time on MR decolorization [conditions: C_0 = 100 mg/L; adsorbent dose = 1 g/100 mL; solution temperature = 25 °C; solution pH = 4]

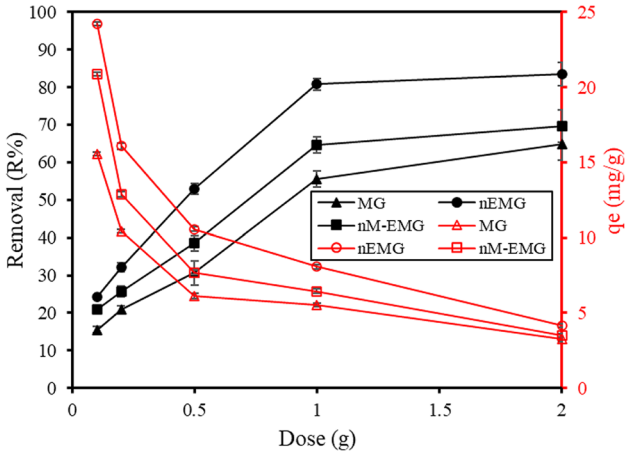

Fig. 9 Effect of adsorbent dose on MR decolorization [conditions: C_0 = 100 mg/L; MR solution volume = 100 mL; solution temperature = 25 °C; solution pH = 4]

pores, where adsorption occurs. However, there may also be a rapid occupation of its lower surface area, hence the short adsorption time and lower adsorption capacity. The nano-eggshell in nEMG has a high surface area with vital oxygen functional groups that are active (sufficiently protonated) at pH 4 and thus improve the adsorption capacity of nEMG. Meanwhile, the introduction of high surface eggshell nano-particles may have delayed the adsorption equilibrium time in nEMG and nM-EMG. Rajoriya et al. [22] reported that MR adsorption on eggshell took 180-min contact time to reach equilibrium. Therefore, the formation of nanoscale eggshell in this work substantially improved the porosity and adsorption capacity of the eggshell (8.1 mg/g) with a relatively lower contact time (40 min) compared to Rajoriya et al. Regarding nM-EMG, the protonated high surface area nano-Fe_3O_4 propelled MR adsorption beyond 40 min where most sites were expected to be occupied. The enhanced diffusion effect by protonated nano-Fe_3O_4 drove the MR adsorption till equilibrium at 60 min, where all active sites were occupied and improved the adsorption capacity of nM-EMG. The equilibrium adsorption capacity of MG, nEMG, and nM-EMG were 5.6, 8.1, and 6.46 mg/g respectively (Fig. 8).

3.2.3 Effect of adsorbent dosage

As illustrated in Fig. 9, increasing the dose of all prepared adsorbents improved MR adsorption efficiency. Increasing the adsorbent dosage above 0.1 g/100 mL expanded the interaction between the dye and the adsorbent surface owing to the increased availability of active adsorption sites due to an increase in total surface area and the number of binding site MR removal on MG, nEMG, and nM-EMG efficiency increased from 15.57 to 68.60%, 24.24 to 87.18%, and 20.84 to 73.50% respectively when the adsorbent dose was increased from 0.1 g/100 mL to 2.0 g/100 mL. Furthermore, increasing the adsorbent dosage increases the number of holes available for MR sorption via pore filling [27, 55]. However, as the adsorbent dosage was increased beyond 0.1 g/100 mL, the equilibrium capacity decreased due to aggregation. Aggregation of adsorbents saturates the adsorption sites, lowering adsorbents' overall effective surface area and lengthening their diffusional path, reducing the adsorption capacity [33, 56]. 1 g/100 mL (10 g/L) was maintained as the optimum dose of all the prepared adsorbents to minimize the agglomeration effect. Moreover, the improvement in MR removal efficiency observed beyond 1 g/100 mL was relatively low.

3.2.4 Effect of initial dye concentration

The adsorption capacities of all prepared adsorbents were enhanced with increasing MR dye concentration as illustrated in Fig. 10. The q_e of MG, nEMG, and nM-EMG increased from 0.92 to 7.90 mg/g, 0.98 to 12.05 mg/g, and 0.93 to 9.44 mg/g respectively when the MR concentration was increased from 10 to 200 mg/L. Increasing dye concentration enhances mass transfer driving force via several collisions between dye molecules and the adsorbents' surface. This phenomenon usually occurs in the initial stages of adsorption [7]. Meanwhile, as MR concentration increased from 10 to 200 mg/L, MG, nEMG, and nM-EMG's adsorption efficiencies declined from 91.93 to 39.50%, 98.49 to 60.23%, and 93.21 to 47.21% respectively. This is possibly due to the growing repulsion forces between the dye molecules on the adsorbent's surface and the bulk phase after the initial rapid adsorption [44]. Furthermore, the ratio

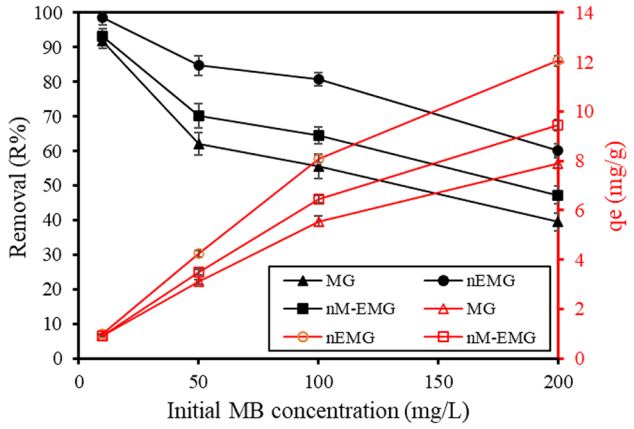

Fig. 10 Effect of initial dye concentration on MR decolorization [conditions: adsorbent dose = 1 g/100 mL; solution temperature = 25 °C; solution pH = 4]

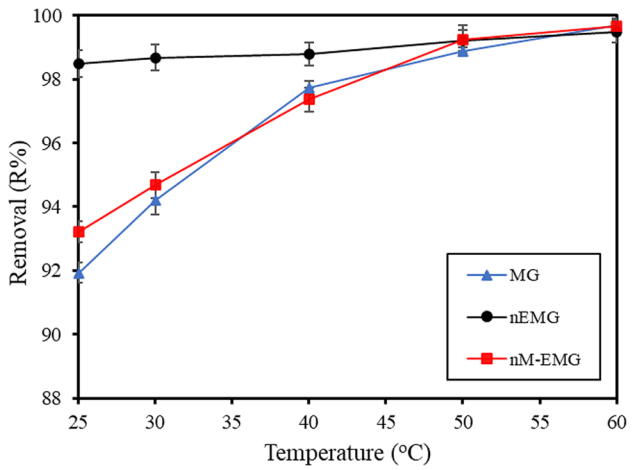

Fig. 11 Effect of solution temperature on MR decolorization [conditions: C_0 = 10 mg/L; adsorbent dose = 1 g/100 mL; solution pH = 4]

of accessible binding sites to the initial dye concentration was greater at lower dye concentrations, implying a high likelihood of complete MR adsorption. Meanwhile, when the initial dye concentration increased, the ratio decreased and there was fast saturation of the adsorption sites, which eventually impeded the further migration of the remaining MR dyestuff towards the adsorbent's surface [7]. Ten milligrams per liter of MR concentration was consequently the optimum concentration where maximum MR removal could be achieved using the prepared adsorbents.

3.2.5 Effect of MR solution temperature

Increasing solution temperature enhanced MR adsorption with all prepared adsorbents as shown in Fig. 11. The MR adsorption on MG, nEMG, and nM-EMG approach complete removal (over 99%) when the temperature was raised to 60 °C. This pattern indicates the presence of strong attractive interactions between adsorbents and MR molecules, implying a chemisorption process [7]. Increasing solution temperature improved MR molecules' diffusion rate from the solution bulk to the adsorbent surface via the external boundary layer and the MR adsorption in the inner pores increased [57]. As temperature rises, the mobility of MR molecules increases while the thickness of the boundary layer surrounding the adsorbent reduces, thus lowering the mass transfer resistance of adsorbate in the boundary layer [57]. Additionally, adsorbents can be activated at elevated temperatures to create new active sites, improving MR adsorption [7]. However, since MR adsorption was stable and effective at 25 °C, 25 °C was selected as the optimum pH. Moreover, increasing temperature can induce extra costs to the adsorption process.

3.3 Adsorption model, kinetics, and mechanism

3.3.1 Adsorption isotherm

The graphs of the linear models of Langmuir, Freundlich, and Temkin isotherms are presented in Fig. S3a, b, c and the values of the isotherm parameters are summarized in Table 2. The maximum Langmuir adsorption capacities (q_m) of 9.11, 13.35, and 10.98 mg/g were obtained with MG, nEMG, and nM-EMG respectively. The R_L values for MG (0.01), nEMG (0.047), and nM-EMG (0.092) were in the range of zero to unity, indicating the MR adsorption processes were favorable. However, MR adsorption with all prepared adsorbents followed the Freundlich isotherm model with a higher coefficient of determination (R^2 = 0.990–0.993) than the Langmuir isotherm model (R^2 = 0.951–0.974). Therefore, the Temkin isotherm was used to check whether the adsorption mechanism is chemisorption [58, 59]. Nevertheless, all MR adsorption systems followed the Temkin model with relatively weak coefficient of determination (R^2 values = 0.872–0.887). Therefore, the Temkin constant (B) could not be used to confirm the adsorption mechanism since the fits were not good enough.

The non-linear Langmuir, Freundlich, Langmuir–Freundlich (L-F), and Dubinin-Radushkevich (D-R) models were fitted on the equilibrium plot of q_e against C_e (Fig. S4) to provide a further understanding of the MR adsorption behavior. From Table 2, both the non-linear Langmuir (R^2 values = 0.978–0.987) and Freundlich (R^2 values = 0.977–0.987) isotherm models of MR adsorption by all prepared adsorbents had strong coefficient of determination. The R^2 values of the L-F isotherm were stronger (0.987–989) than that of the non-linear Langmuir, Freundlich, and D-R models. This confirms that the L-F isotherm better describes the MR adsorption process. The L-F isotherm describes the

Table 2 Adsorption isotherm parameters of MR-adsorbent systems at an adsorbent dosage of 1 g/100 mL, pH of 4, and temperature of 25 °C

Adsorption isotherm	Parameter	MG	nEMG	nM-EMG
Langmuir (linear)	q_m (mg/g)	9.11	13.35	10.98
	k_L (L/mg)	0.044	0.102	0.049
	R_L	0.010	0.047	0.092
	R^2	0.974	0.972	0.951
Freundlich (linear)	k_F (mg/g)	0.981	2.099	1.100
	$1/n_F$	0.433	0.407	0.466
	R^2	0.991	0.990	0.993
Temkin	k_T (L/g)	1.657	6.969	1.727
	B (J/mol)	1.310	1.664	1.598
	R^2	0.883	0.872	0.887
Langmuir (non-linear)	q_{nm} (mg/g)	0.932	2.529	1.396
	k_{nL} (L/mg)	4.374	6.104	2.587
	R^2	0.987	0.978	0.986
Freundlich (non-linear)	k_{nF} (mg/g)	0.935	2.290	1.168
	n_F	0.448	0.384	0.452
	R^2	0.987	0.977	0.985
Langmuir–Freundlich	q_{mLF} (mg/g)	31.33	13.696	20.144
	k_{LF} (L/mg)	0.00113	0.06891	0.00804
	n_{LF}	0.539	1.181	0.667
	R^2	0.988	0.987	0.989
Dubinin-Radushkevich	q_{DR} (mg/g)	5.545	11.276	8.980
	k_{DR}	2.870	72.746	250.02
	R^2	0.527	0.947	0.943
	$\beta_{ad} \times 10^{-7}$	4.68	118.51	407.31
	E (kJ/mol)	1.034	0.205	0.111

adsorption process as Langmuir (chemisorption) but with the distribution of adsorption energy onto a heterogeneous adsorbent surface [59, 60].

3.3.2 MR adsorption kinetics

For all prepared adsorbents, MR adsorption followed the pseudo-second-order kinetics model with R^2 closer to unity than the pseudo-first-order kinetics model (Table 3). Moreover, the calculated equilibrium adsorption capacities (q_e, cal) of the pseudo-second-order kinetics model were closer to the actual equilibrium adsorption capacities (relatively low $\Delta q(\%)$ values). Therefore, the rate-controlling step for all MR sorption systems may be chemisorption [33, 60]. Furthermore, these findings indicate that the MR dye adsorption rate depended on the surface area of the produced adsorbents and the availability of adsorptive sites [44, 61]. The MR chemisorption is portrayed by the electrostatic interaction between the protonated oxygen functional groups of the adsorbents and the COO^- group of MR as illustrated in Fig. 6. Meanwhile, k_2 values dropped as the dye concentration increased due to stronger competition for the adsorptive sites with increasing dye concentration.

3.3.3 MR diffusion mechanism

Generally, the rate of adsorption can be controlled by various factors such as (a) adsorbate ion diffusion from the solution phase to the film surrounding the external surface of the adsorbent (film diffusion); (b) diffusion from the film to the particle surface (external diffusion); (c) diffusion from the surface to the internal sites (surface diffusion or pore diffusion); and (d) adsorbate ion uptake via physicochemical adsorption, ion exchange, precipitation, or complexation [43]. The kinetics of all MR adsorption processes were first elucidated using intra-particle diffusion and comprised two phases (Fig. S5). The first phase involved (a) and (b) simultaneously and the final steps involved (c) and (d). From Fig. S5, the intra-particle diffusion model is not the only control mechanism, as the multi-linear plots of q_t versus $t^{0.5}$ of all adsorption systems did not pass through the origin [32, 43]. Moreover, the R^2 values of intra-particle diffusion are between 0.685 and 0.740 for MG, 0.737 and 0.850 for nEMG, and 0.752 and 878 for nM-EMG (Table 3). The thickness of the boundary layer (C) was between 0.19 and 3.59 for MG, 0.20 and 2.85 for nEMG, and 0.23–3.17 for nM-EMG.

Meanwhile, the film diffusion model (plot of $\ln[1 - q_t/q_e]$ against t) for all prepared adsorbents (Fig. S6) had a stronger linear correlation in ranges of 0.952–0.998, 0.918–0.980, and 0.949–0.994 for MG, nEMG, and nM-EMG respectively (Table 3). This shows that the film diffusion model is applicable. However, if the film diffusion is only the rate control step, its plot should be linear with zero intercept [43]. Since the linear plots of the film diffusion model did not pass through the origin, the liquid-film diffusion model may not be the only rate-controlling step. Consequently, intra-particle diffusion and liquid-film diffusion controlled the MR dye adsorption on all prepared adsorbents. The liquid-film rate constants, k_{lfd}, were between 0.070 and 0.123 min^{-1} for MG, 0.074–0.108 for nEMG, and 0.061–4.805 min^{-1} for nM-EMG (Table 3).

3.3.4 Thermodynamics studies of MR adsorption

The thermodynamic fit of MR-adsorbent systems and the results of the thermodynamic parameters are presented in Fig. S7 and Table 4 respectively. The ΔH values were positive; hence, all adsorption processes were endothermic with all adsorbents. In all the MR adsorption systems, negative ΔG values indicated that adsorbent processes were spontaneous and feasible. In addition, the ΔG values decreased with the increase in temperatures indicating that the process of adsorption was more spontaneous with temperature and

Table 3 Parameters and coefficients of the kinetic models of MR-sorption systems at a temperature of 25 °C, pH of 4, and adsorbents dose of 1 g/100 mL

C_0 (mg/L)		10			50			100			200		
Adsorbents		MG	nEMG	nM-EMG	MG	nEMG	nM-EMG	MG	nEMG	nM-EMG	MG	nEMG	nM-EMG
q_e, exp		0.92	0.98	0.93	3.10	4.24	3.51	5.55	8.08	6.46	7.90	12.05	9.44
PFO	q_e, cal	1.01	1.18	1.80	3.43	3.81	3.36	5.68	9.01	7.73	8.22	15.50	8.79
	k_1	0.070	0.074	4.805	0.094	0.076	0.933	0.093	0.087	0.463	0.123	0.104	0.061
	R^2	0.952	0.980	0.949	0.967	0.980	0.986	0.998	0.956	0.957	0.992	0.918	0.992
	$\Delta q(\%)$	6.693	11.37	41.76	7.479	5.865	1.887	1.621	6.672	8.834	2.817	16.55	3.075
PSO	q_e, cal	1.03	1.20	1.02	3.31	4.47	3.80	5.83	8.69	7.57	8.20	13.25	10.60
	k_2	0.970	0.830	0.982	0.302	0.223	0.263	0.172	0.115	0.132	0.122	0.075	0.094
	R^2	0.974	0.997	0.993	0.991	0.998	0.997	0.996	0.994	0.988	0.998	0.992	0.999
	$\Delta q(\%)$	8.620	12.88	4.130	4.736	3.213	3.735	3.524	4.383	7.738	2.701	5.764	5.504
ELV	β	4.514	4.190	5.350	1.720	1.602	1.516	1.155	0.644	0.582	0.953	0.395	0.532
	α	0.217	0.264	0.414	1.884	1.866	1.865	8.165	4.095	0.922	29.81	4.571	3.825
	R^2	0.686	0.905	0.703	0.653	0.818	0.831	0.683	0.775	0.906	0.685	0.763	0.939
IPD	C	0.19	0.20	0.23	3.59	2.75	3.17	1.66	2.02	0.87	2.56	2.85	2.12
	K_{ipd}	0.09	0.10	0.09	0.28	0.36	0.31	0.48	0.73	0.63	0.66	1.12	0.87
	R^2	0.740	0.850	0.752	0.714	0.737	0.783	0.706	0.766	0.878	0.685	0.770	0.838
LFD	K_{lfd}	0.070	0.074	4.805	0.094	0.076	0.933	0.093	0.087	0.463	0.123	0.104	0.061
	R^2	0.952	0.980	0.949	0.967	0.980	0.994	0.998	0.956	0.957	0.992	0.918	0.992

Table 4 Thermodynamics parameters of prepared adsorbents on the adsorption of 100 mg/L of MR dye at temperatures of 25 to 60 °C, pH of 4, and adsorbent dose of 1 g/100 mL

Adsorbent	Temperature (°C)	25	30	40	50	60
MG	ΔG (kJ/mol)	−0.32	−1.22	−3.81	−5.82	−9.69
	ΔH (kJ/mol)	77.27				
	ΔS (J/mol/K)	259.36				
nEMG	ΔG (kJ/mol)	−4.65	−5.07	−5.47	−6.79	−8.13
	ΔH (kJ/mol)	24.24				
	ΔS (J/mol/K)	96.38				
nM-EMG	ΔG (kJ/mol)	−0.79	−1.45	−3.40	−6.92	−9.36
	ΔH (kJ/mol)	74.86				
	ΔS (J/mol/K)	252.38				

chemisorption [7]. The positive ΔS values denote that the degree of randomness of the adsorption process increased at the solid–liquid interface [32]. The positive ΔS values also suggest a solvent-replacing phenomenon in the sorption process, in which the MR molecules replace water molecules on the adsorbents' surface [44].

3.4 Performance of prepared adsorbents in different water matrices

Several inorganic ions are ubiquitously present in natural waters along with natural organic matter (humic acid (HA)) and suspended solids. Highly turbid water can lead to poor mixing between adsorbents and adsorbate and slow down the mobility of adsorbate ions onto the adsorbent's surface. Inorganic ions such as chlorides and sulfates (high total dissolved solids (TDS)) can compete with adsorbate for the adsorbent's active site and decrease the adsorption capacity. High specific ultraviolet absorbance (SUVA) values (≥ 2.0 L/mg m) signify the high aromaticity of the organic content [62]. The natural organic matter (NOM) from dissolved organic carbon (DOC) of high aromatic content can be adsorbed on the surface of the adsorbents via π electron interactions or biosorption and exhaust the active sites needed for adsorbate adsorption. Thus, the prepared adsorbents were tested for their selectivity towards MR dye in different water matrices (Fig. S8). Ten parts per million MR solution was prepared in 100 mL of distilled water (DIW), tap water (TW), seawater (SW), lake water (LW), and drain water (DW) under the optimum condition (adsorbent dose of 1.0 g/100 mL and pH 4) for 60 min. The characteristics of the water matrix are described in Table S1.

The adsorption capacity of MG dropped from 7.903 mg/g in DIW to 7.09 mg/g in TW, 4.23 mg/g in SW, 6.19 mg/g in LW, and 4.41 in DW. nEMG's adsorption capacity decreased from 12.196 mg/g in DIW to 10.92 mg/g in TW, 7.61 mg/g in SW, 8.98 mg/g in LW, and 5.88 in DW. nM-EMG's capacity for MR reduced from 9.44 mg/g in DIW to 8.92 mg/g in TW, 6.823 mg/g in SW, 7.98 mg/g in LW, and 7.69 mg/g in DW. As illustrated in Fig. S8, DIW and TW had a mild influence on the selectivity of all prepared adsorbents towards MR. TW and DIW contain relatively low TDS, low DOC, and low turbidity. Thus, competition for adsorbents' active sites in such waters was minimal. Although LW also has low TDS, the adsorption capacity of all the prepared adsorbents dropped. This decrease in adsorption capacity was attributed to lake water's high turbidity, resulting in poor mobility of MR ions. Moreover, the adsorption capacity of nEMG was greatly affected compared to MG and nM-EMG. This outcome is ascribed to the relatively high DOC of lake water. Biosorption of the DOC by the bio-$CaCO_3$ of eggshell in nEMG may have reduced the total active sites and affinity for MR ions. Meanwhile, the nano-magnetic coating of nM-EMG reduced its biosorption affinity and improved nM-EMG performance in high DOC waters. The lowest MR adsorption efficiencies were attained in the case of SW, followed by the DW water matrix due to the presence of inorganic salts and high turbidity in these water matrices. This study showed that the adsorption efficiency was influenced by dissolved inorganic salts, turbidity, and organic matter. However, the influence on nM-EMG was relatively less, possibly due to the nano-Fe_3O_4 coating serving as a layer that reduced the competition for oxygen functional groups such as the O–H, C = O, and C–O.

3.5 Recyclability of adsorbents

The efficiency of the MR removal after regeneration and reuse of produced adsorbents is shown in Fig. 12. The efficiency of MR adsorption declined from 91.7% (cycle 1) to 72.2% (cycle 5) and 98.2% (cycle 1) to 71.1% (cycle 5) for MG and nEMG, respectively. This is due to the loss of MG and nEMG during the collection of adsorbents via filtration and centrifugation. Meanwhile, the removal efficiency decreased from 93.2% (cycle 1) to 89.7% (cycle 5) with nM-EMG. The decline in removal efficiency of nM-EMG was less than MG and nEMG. This outcome reveals the high stability and reusability of nM-EMG because of the easy and effective magnetic separation and negligible adsorbent loss during collection. Hence, the nano-magnetization overcame the problem of particle collection after adsorption and the occurrence of secondary pollution. Moreover, it saves the time and energy required to collect particles via filtration and centrifugation.

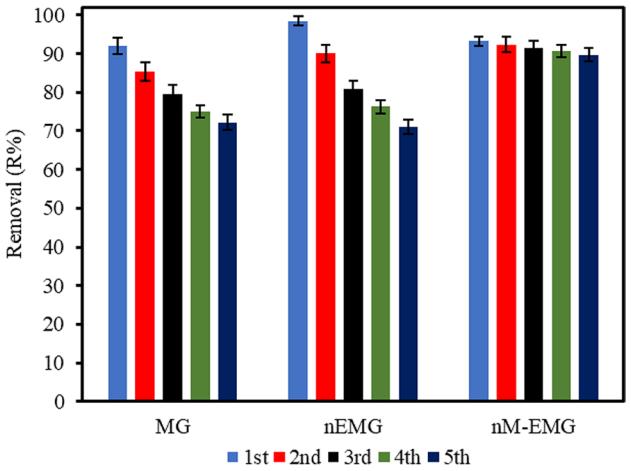

Fig. 12 Reusability of adsorbents [conditions: $C_0 = 10$ mg/L; adsorbent dose = 1 g/100 mL; temperature = 25 °C; solution pH = 4]

3.6 Comparison of MR adsorption studies

Table S2 compares this present study with literature under different experimental conditions of MR adsorption. MG, nEMG, and nM-EMG showed higher adsorption performance than the adsorbents prepared in other studies [22, 32, 43, 46, 63–68]. However, other adsorbents with higher MR adsorption capacity than the prepared adsorbents in this work were chemically modified using reagents such as K_2CO_3, H_2SO_4, H_3PO_4, and KOH. Besides the implications of additional costs, these chemicals can also be potentially toxic to the environment. Thus, this work's utilization of waste plastics and eggshells offers an innovative, facile, green, and cheap technology to prepare novel adsorbents for effective wastewater decontamination.

4 Conclusion

The interaction between the components of the composites, chemical structure, chemical composition, high surface area, and high porosity was affirmed by the performed analyses. nEMG has an improved surface area, porosity, and adsorption capacity due to nano-eggshell modification. The MR adsorption occurred via electrostatic interactions, π-π electron stacking, π-π electron or donor–acceptor interactions, and hydrogen bonding. MR adsorption was more favored at low pH ranges ($3 < pH < 6$), where strong electrostatic interactions occurred between the COO^- group of zwitterionic $MR^{\pm}$ and the positively charged adsorbents' surface. The optimum values of pH, initial MR concentration, adsorbent dose, and temperature were 4, 10 mg/L, 1 g/100 mL, and 25 °C respectively. The MR adsorption on MG, nEMG, and nM-EMG reached equilibrium at 30, 40, and 60 min

respectively. MR removal efficiency with MG, nEMG, and nM-EMG declined from 91.93 to 39.50%, 98.49 to 60.23%, and 93.21 to 47.21% respectively when the MR concentration increased from 10 to 200 mg/L. The adsorption process was chemical, spontaneous, and endothermic and was governed by intra-particle and film diffusion. nM-EMG showed exhibited excellent stability and reusability than MG and nEMG with MR removal decreasing from 93.2 to 89.7% after five repetitive cycles. The influence of co-adsorbates or impurities such as organic matter and dissolved solids in different water matrices on nM-EMG was relatively low due to nano-Fe_3O_4 layer. The prepared magnetic nano-eggshell modified carbon composite (nM-EMG) in this work is a cost-efficient, green, and effective adsorbent and can be efficiently recycled in repetitive cycles which qualifies the prepared composite to be applied on a wider scale. The adsorbents prepared in this work have low chemical demand, thus reducing cost, the complexity of chemical handling, and chemical toxicity to the environment. Valorizing waste plastics and eggshells proposed in this work offers a profitable opportunity to curb the environmental menace associated with these wastes. Further research is needed to optimize the ratios between nano-eggshell and MG, and between iron concentration and nEMG, as well as an economic analysis.

Supplementary Information The online version contains supplementary material available at https://doi.org/10.1007/s13399-022-03304-4.

Author contribution KM contributed to the study conception and design. Material preparation, data collection, and analysis were performed by KM. The first draft of the manuscript was written by KM and all authors commented on previous versions of the manuscript. MS, HS, HM, and MF revised the manuscript. HS, HM, and MF supervised the work. All authors read and approved the final manuscript.

Funding Open access funding provided by The Science, Technology & Innovation Funding Authority (STDF) in cooperation with The Egyptian Knowledge Bank (EKB).

Data availability All data and materials generated or analyzed during this study are included in this published article (and its supplementary information files).

Declarations

Ethics approval This article does not contain any studies with human participants or animals performed by any of the authors.

Competing interests The authors declare no competing interests.

References

1. El Hassani K, Kalnina D, Turks M et al (2019) Enhanced degradation of an azo dye by catalytic ozonation over Ni-containing layered double hydroxide nanocatalyst. Sep Purif Technol 210:764–774. https://doi.org/10.1016/j.seppur.2018.08.074
2. Shindhal T, Rakholiya P, Varjani S et al (2021) A critical review on advances in the practices and perspectives for the treatment of dye industry wastewater. Bioengineered 12:70–87
3. Carmen Z, Daniel S (2012) Textile organic dyes – characteristics, polluting effects and separation/elimination procedures from industrial effluents – a critical overview. Org Pollut Ten Years After Stock Conv - Environ Anal Updat. https://doi.org/10.5772/32373
4. Sadeghi A, Esfandiari N, Honarvar B, et al (2022) Investigation of lead adsorption from synthetic effluents by modified activated carbon particles using the response surface methodology. Biomass Convers Biorefinery 1–12. https://doi.org/10.1007/S13399-022-02585-Z
5. Samy M, Alalm MG, Mossad M (2020) Utilization of iron sludge resulted from electro-coagulation in heterogeneous photo-fenton process. Water Pract Technol 15:1228–1237. https://doi.org/10.2166/wpt.2020.093
6. Wang B, Wang Y (2022) A comprehensive review on persulfate activation treatment of wastewater. Sci Total Environ 154906. https://doi.org/10.1016/J.SCITOTENV.2022.154906
7. Mensah K, Mahmoud H, Fujii M, Shokry H (2022) Novel nano-ferromagnetic activated graphene adsorbent extracted from waste for dye decolonization. J Water Process Eng 45:102512–102523. https://doi.org/10.1016/j.jwpe.2021.102512
8. Isik Z, Saleh M, M'barek I, et al (2022) Investigation of the adsorption performance of cationic and anionic dyes using hydrochared waste human hair. Biomass Convers Biorefinery 1–14. https://doi.org/10.1007/S13399-022-02582-2
9. Luan P, Liao J, Chen L, et al (2022) Facile and sustainable modification for improving the adsorption ability of sugarcane bagasse towards cationic organic pollutants. Biomass Convers Biorefinery 1–16. https://doi.org/10.1007/S13399-022-02551-9
10. Motejadded Emrooz HB, Maleki M, Rashidi A, Shokouhimehr M (2020) Adsorption mechanism of a cationic dye on a biomass-derived micro- and mesoporous carbon: structural, kinetic, and equilibrium insight. Biomass Convers Biorefinery 11:943–954. https://doi.org/10.1007/S13399-019-00584-1
11. Patel P, Gupta S, Mondal P (2022) Modeling and optimization of process parameters of MB dye adsorption using waste-derived chemically activated biosorbents. Biomass Convers Biorefinery 1–20. https://doi.org/10.1007/S13399-022-02693-W
12. Oladipo, B, Ibrahim, TH, Ajala, SO, Akintunde, AM, Taiwo, AE, Betiku, E (2021). Synthesis of Activated Carbons for Heavy Metals Removal. In: Inamuddin, Ahamed, M., Lichtfouse, E., Asiri, A. (eds) Green Adsorbents to Remove Metals, Dyes and Boron from Polluted Water. Environmental Chemistry for a Sustainable World. Springer, Cham. 49:1–31. https://doi.org/10.1007/978-3-030-47400-3_1
13. Nimako KO, Dwumfour A, Mensah K et al (2020) Calcination behaviour of Nsuta Rhodochrosite ore in the presence and

absence of end-of-life high density polyethylene. Ghana Min J 20:22–35. https://doi.org/10.4314/gm.v20i2.4
14. Dankwah JR, Yussif I, Hinson OS et al (2018) Application of microwave technology to the production of iron nuggets from the Sheini iron ore using mixed plastics waste as reductants *. Ghana J Technol 2:79–87
15. Thushari GGN, Senevirathna JDM (2020) Plastic pollution in the marine environment. Heliyon 6:e04709. https://doi.org/10.1016/j.heliyon.2020.e04709
16. Thakur S, Singh S, Pal B (2021) Superior adsorptive removal of brilliant green and phenol red dyes mixture by CaO nanoparticles extracted from egg shells. J Nanostructure Chem. https://doi.org/10.1007/s40097-021-00412-x
17. Hassan TA, Rangari VK, Rana RK, Jeelani S (2013) Sonochemical effect on size reduction of CaCO3 nanoparticles derived from waste eggshells. Ultrason Sonochem 20:1308–1315. https://doi.org/10.1016/j.ultsonch.2013.01.016
18. Tsai WT, Hsien KJ, Hsu HC et al (2008) Utilization of ground eggshell waste as an adsorbent for the removal of dyes from aqueous solution. Bioresour Technol 99:1623–1629. https://doi.org/10.1016/j.biortech.2007.04.010
19. Faridi H, Arabhosseini A (2018) Application of eggshell wastes as valuable and utilizable products: a review. Res Agric Eng 64:104–114. https://doi.org/10.17221/6/2017-RAE
20. Annane K, Lemlikchi W, Tingry S (2021) Efficiency of eggshell as a low-cost adsorbent for removal of cadmium: kinetic and isotherm studies. Biomass Convers Biorefinery. https://doi.org/10.1007/s13399-021-01619-2
21. Abdel-Khalek MA, Abdel Rahman MK, Francis AA (2017) Exploring the adsorption behavior of cationic and anionic dyes on industrial waste shells of egg. J Environ Chem Eng 5:319–327. https://doi.org/10.1016/j.jece.2016.11.043
22. Rajoriya S, Saharan VK, Pundir AS et al (2021) Adsorption of methyl red dye from aqueous solution onto eggshell waste material: kinetics, isotherms and thermodynamic studies. Curr Res Green Sustain Chem 4:100180. https://doi.org/10.1016/j.crgsc.2021.100180
23. Slimani R, El Ouahabi I, Abidi F et al (2014) Calcined eggshells as a new biosorbent to remove basic dye from aqueous solutions: thermodynamics, kinetics, isotherms and error analysis. J Taiwan Inst Chem Eng 45:1578–1587. https://doi.org/10.1016/j.jtice.2013.10.009
24. Katha PS, Ahmed Z, Alam R et al (2021) Efficiency analysis of eggshell and tea waste as low cost adsorbents for Cr removal from wastewater sample. South African J Chem Eng 37:186–195. https://doi.org/10.1016/j.sajce.2021.06.001
25. Wang H, Gao B, Fang J et al (2018) Engineered biochar derived from eggshell-treated biomass for removal of aqueous lead. Ecol Eng 121:124–129. https://doi.org/10.1016/j.ecoleng.2017.06.029
26. Mensah K, Abdelmageed AM, Shokry H (2022) Effect of eggshell/N, N-dimethylformamide (DMF) mixing ratios on the sonochemical production of CaCO3 nanoparticles. J Eng Appl Sci 69:1–12. https://doi.org/10.1186/s44147-022-00070-y
27. Mashkoor F, Nasar A (2020) Magsorbents: potential candidates in wastewater treatment technology – a review on the removal of methylene blue dye. J Magn Magn Mater 500:166408. https://doi.org/10.1016/j.jmmm.2020.166408
28. Panda SK, Aggarwal I, Kumar H et al (2021) Magnetite nanoparticles as sorbents for dye removal: a review. Environ Chem Lett 19:2487–2525. https://doi.org/10.1007/s10311-020-01173-9
29. Wong KT, Eu NC, Ibrahim S et al (2016) Recyclable magnetite-loaded palm shell-waste based activated carbon for the effective removal of methylene blue from aqueous solution. J Clean Prod 115:337–342. https://doi.org/10.1016/j.jclepro.2015.12.063
30. Gar Alalm M, Tawfik A, Ookawara S (2016) Solar photocatalytic degradation of phenol by TiO2/AC prepared by temperature impregnation method. Desalin Water Treat 57:835–844. https://doi.org/10.1080/19443994.2014.969319
31. Liu S, Yu B, Wang S et al (2020) Preparation, surface functionalization and application of Fe3O4 magnetic nanoparticles. Adv Colloid Interface Sci 281:102165. https://doi.org/10.1016/j.cis.2020.102165
32. Khan EA, Shahjahan KTA (2018) Adsorption of methyl red on activated carbon derived from custard apple (Annona squamosa) fruit shell: equilibrium isotherm and kinetic studies. J Mol Liq 249:1195–1211. https://doi.org/10.1016/j.molliq.2017.11.125
33. El Essawy NA, Ali SM, Farag HA et al (2017) Green synthesis of graphene from recycled PET bottle wastes for use in the adsorption of dyes in aqueous solution. Ecotoxicol Environ Saf 145:57–68. https://doi.org/10.1016/j.ecoenv.2017.07.014
34. Rai P, Singh KP (2018) Valorization of poly (ethylene) terephthalate (PET) wastes into magnetic carbon for adsorption of antibiotic from water: characterization and application. J Environ Manage 207:249–261. https://doi.org/10.1016/j.jenvman.2017.11.047
35. Thommes M, Kaneko K, Neimark AV et al (2015) Physisorption of gases, with special reference to the evaluation of surface area and pore size distribution (IUPAC Technical Report). Pure Appl Chem 87:1051–1069. https://doi.org/10.1515/pac-2014-1117
36. Kumar KV, Gadipelli S, Wood B et al (2019) Characterization of the adsorption site energies and heterogeneous surfaces of porous materials. J Mater Chem A 7:10104–10137. https://doi.org/10.1039/c9ta00287a
37. Khan B, Nawaz M, Waseem M, et al (2019) Adsorption of methylene blue onto size controlled magnetite nanoparticles. Mater Res Express 6.https://doi.org/10.1088/2053-1591/ab2ef9
38. Shen Y, Lua AC (2013) A facile method for the large-scale continuous synthesis of graphene sheets using a novel catalyst. Sci Rep 3:1–6. https://doi.org/10.1038/srep03037
39. Zhou G-T, Yao Q-Z, Fu S-Q, Guan Y-B (2010) Controlled crystallization of unstable vaterite with distinct morphologies and their polymorphic transition to stable calcite. Eur J Mineral 22:259–269. https://doi.org/10.1127/0935-1221/2009/0022-2008
40. Chowdhury S, Chakraborty S, Das SP (2013) Removal of crystal violet from aqueous solution by adsorption onto eggshells: equilibrium, kinetics, thermodynamicsand artificial neural network modeling. Waste Biomass Valorization 4:655–664. https://doi.org/10.1007/s12649-012-9139-1
41. Chowdhury S, Papita D (2014) Utilization of a domestic waste—eggshells for removal of hazardous malachite green from aqueous solutions. Environ Prog Sustain Energy 33:676–680. https://doi.org/10.1002/ep.10564
42. Ge H, Wang C, Liu S, Huang Z (2016) Synthesis of citric acid functionalized magnetic graphene oxide coated corn straw for methylene blue adsorption. Bioresour Technol 221:419–429. https://doi.org/10.1016/j.biortech.2016.09.060
43. Ahmad MA, Ahmad N, Bello OS (2015) Modified durian seed as adsorbent for the removal of methyl red dye from aqueous solutions. Appl Water Sci 5:407–423. https://doi.org/10.1007/s13201-014-0208-4
44. Shokry H, Elkady M, Hamad H (2019) Nano activated carbon from industrial mine coal as adsorbents for removal of dye from simulated textile wastewater: operational parameters and mechanism study. J Mater Res Technol 8:4477–4488. https://doi.org/10.1016/j.jmrt.2019.07.061
45. Kumi AG, Ibrahim MG, Fujii M, Nasr M (2020) Synthesis of sludge-derived biochar modified with eggshell waste for monoethylene glycol removal from aqueous solutions. SN Appl Sci 2:1–12. https://doi.org/10.1007/s42452-020-03501-8

46. Saleh TA, Al-Absi AA (2017) Kinetics, isotherms and thermodynamic evaluation of amine functionalized magnetic carbon for methyl red removal from aqueous solutions. J Mol Liq 248:577–585. https://doi.org/10.1016/j.molliq.2017.10.064
47. Benedict JB, Cohen DE, Lovell S et al (2006) What is syncrystallization? States of the pH indicator methyl red in crystals of phthalic acid. J Am Chem Soc 128:5548–5559. https://doi.org/10.1021/ja0601181
48. Rápó E, Aradi LE, Szabó Á et al (2020) Adsorption of remazol brilliant violet-5R textile dye from aqueous solutions by using eggshell waste biosorbent. Sci Rep 10:1–12. https://doi.org/10.1038/s41598-020-65334-0
49. Ngadi N, Ee CC, Yuszff NA (2013) Removal of methylene blue dye by using eggshell powder. J Teknol Sci Eng 65:63–71. https://doi.org/10.11113/jt.v65.1648
50. Dong H, Fredrickson JK, Kennedy DW et al (2000) Mineral transformation associated with the microbial reduction of magnetite. Chem Geol 169:299–318. https://doi.org/10.1016/S0009-2541(00)00210-2
51. Anthony JW, Bideaux RA, Bladh KW, Nichols MC (eds) (2003) Handbook of Mineralogy. Mineralogical Society of America, Chantilly, VA 20151-1110, USA. http://www.handbookofmineralogy.org/
52. Tzeng TW, Liu YT, Deng Y et al (2016) Removal of sulfamethazine antibiotics using cow manure-based carbon adsorbents. Int J Environ Sci Technol 13:973–984. https://doi.org/10.1007/s13762-015-0929-4
53. Teixido M, Pignatello J, Beltran J et al (2011) Speciation of the ionizable antibiotic sulfamethazine on black carbon (biochar). Environ Sci Technol 45(10020–10027):10020–10027. https://doi.org/10.1021/es202487h
54. Liu Y, Liu X, Dong W et al (2017) Efficient adsorption of sulfamethazine onto modified activated carbon: a plausible adsorption mechanism. Sci Rep 7:1–12. https://doi.org/10.1038/s41598-017-12805-6
55. Ai L, Zhang C, Chen Z (2011) Removal of methylene blue from aqueous solution by a solvothermal-synthesized graphene/magnetite composite. J Hazard Mater 192:1515–1524. https://doi.org/10.1016/j.jhazmat.2011.06.068
56. Altıntıg E, Altundag H, Tuzen M, Sari A (2017) Effective removal of methylene blue from aqueous solutions using magnetic loaded activated carbon as novel adsorbent. Chem Eng Res Des. https://doi.org/10.1016/j.cherd.2017.03.035
57. El Essawy NA, Konsowa AH, Elnouby M, Farag HA (2017) A novel one-step synthesis for carbon-based nanomaterials from polyethylene terephthalate (PET) bottles waste. J Air Waste Manag Assoc 67:358–370. https://doi.org/10.1080/10962247.2016.1242517
58. Boparai HK, Joseph M, O'Carroll DM (2011) Kinetics and thermodynamics of cadmium ion removal by adsorption onto nano zerovalent iron particles. J Hazard Mater 186:458–465. https://doi.org/10.1016/j.jhazmat.2010.11.029
59. Al-Ghouti MA, Da'ana DA (2020) Guidelines for the use and interpretation of adsorption isotherm models: a review. J Hazard Mater 393:122383. https://doi.org/10.1016/j.jhazmat.2020.122383
60. Ayawei N, Ebelegi AN, Wankasi D (2017) Modelling and interpretation of adsorption isotherms. J Chem 2017. https://doi.org/10.1155/2017/3039817
61. Sahoo TR, Prelot B (2020) Chapter 7 - Adsorption processes for the removal of contaminants from wastewater: the perspective role of nanomaterials and nanotechnology. In: Bonelli B, Freyria FS, Rossetti I, Sethi R (eds) Nanomaterials for the Detection and Removal of Wastewater Pollutants. Elsevier 161–222. https://doi.org/10.1016/B978-0-12-818489-9.00007-4
62. Samy M, Gar Alalm M, Fujii M, Ibrahim MG (2021) Doping of Ni in MIL-125(Ti) for enhanced photocatalytic degradation of carbofuran: reusability of coated plates and effect of different water matrices. J Water Process Eng 44:102449. https://doi.org/10.1016/j.jwpe.2021.102449
63. Santhi T, Manonmani S, Smitha T (2010) Removal of methyl red from aqueous solution by activated carbon prepared from the *Annona squmosa* seed by adsorption. Chem Eng Res Bull 14:11–18. https://doi.org/10.3329/cerb.v14i1.3767
64. Ioannou Z, Karasavvidis C, Dimirkou A, Antoniadis V (2013) Adsorption of methylene blue and methyl red dyes from aqueous solutions onto modified zeolites. Water Sci Technol 67:1129–1136. https://doi.org/10.2166/wst.2013.672
65. Haris MRHM, Sathasivam K (2009) The removal of methyl red from aqueous solutions using banana pseudo stem fibers. Am J Appl Sci 6:1690–1700
66. Ghaedi M, Kokhdan SN (2012) Oxidized multiwalled carbon nanotubes for the removal of methyl red (MR): kinetics and equilibrium study. New pub Balaban 49:317–325. https://doi.org/10.1080/19443994.2012.719355
67. Saad SA, Isa KM, Bahari R (2010) Chemically modified sugarcane bagasse as a potentially low-cost biosorbent for dye removal. Desalination 264:123–128. https://doi.org/10.1016/j.desal.2010.07.015
68. Shariati-Rad M, Irandoust M, Amri S et al (2014) Removal, preconcentration and determination of methyl red in water samples using silica coated magnetic nanoparticles. Int Nano Lett 4:91–101. https://doi.org/10.1007/s40089-014-0124-5